RGNZ/MGPB

Chemical and textural studies of the youngest pyroclastic deposits at Mt. Seminung (South Sumatra, Indonesia): A window for understanding the explosive behavior of a post-caldera volcano

Rachmi Mustika Pertiwi Putri Gunawan[1,2]; **Indranova Suhendro** [2,3,4]

[1] Balai Besar Pengujian Minyak dan Gas Bumi LEMIGAS, Ministry of Energy and Mineral Resources, Jl. Ciledug Raya, Kav. 109, Cipulir, Kebayoraan Lama, Jakarta Selatan, DKI Jakarta 12230, Indonesia.

[2] Department of Earth and Planetary Sciences, Graduate School of Science, Kyushu University, Nishiku, 744, Motooka, Fukuoka, 819-3095, Japan.

[3] Department of Environmental Geography, Faculty of Geography, Universitas Gadjah Mada, Sekip Utara, Jl. Kaliurang, Bulaksumur, Yogyakarta 55281, Indonesia.

[4] Center for Disaster Studies, Universitas Gadjah Mada, Jl. Mahoni C-16, Bulaksumur, Yogyakarta, Indonesia.

Abstract

The youngest tephra deposits of Seminung Volcano in South Sumatra, Indonesia, was studied by addressing the stratigraphy (field data), componentry, petrography, glass and mineral compositions, and textural analysis of vesicles to interpret the magmatic system and eruption dynamics. Based on the componentry and grain size characteristics, the section is divided into three different units: (1) massive block and ash, (2) interbedded ash and lapilli, and (3) massive lapilli. All units include grey pumice (GP), brown pumice (BP), and scoria (SC) as the main juvenile types, while porphyritic lava occurs as the non-juvenile phase (lithics). Noteworthy, minor banded pumice (BaP) can be observed in all units, and accretionary lapilli (AL) is exclusive in the interbedded ash and lapilli unit. The similarity in mineralogy and the linear correlation of all major elements of glass compositions suggest that grey and brown pumice originated from the same shallow, biotite-bearing more silicic magma (64.5-74.9 wt. %), while scoria originates from the deeper, biotite-free less silicic magma (62.1-69.2 wt. %). The fact that grey pumice shows higher silica content and pheno-bubble fraction with lower phenocryst content than brown pumice suggests the rough stratification of the more silicic magma reservoir. Furthermore, the more silicic magma was likely intruded by the deeper less silicic magma, as indicated by the bimodal distribution of anorthite (An#) in grey and brown pumices (i.e. the peak of the high anorthite content is similar to that of scoria). Thus, the accumulation of pheno-bubble and magmatic recharge were likely responsible for triggering the eruption. Finally, the fact that juvenile clasts from units 2 and 3 had the highest matrix-vesicle number density (MVND) implies that the eruption intensity reached its peak towards the final eruption stage.

Keywords:

Seminung; magma mingling; magma stratification; overpressure; pheno-bubble; matrix-bubble

1. Introduction

Indonesia is a volcano-rich country; it has 127 active and abundant (uncounted or undocumented) dormant volcanoes with their related hazard potentials. Most of the volcanological studies conducted in Indonesia focus on studying active volcanoes; thus, our knowledge of the potential risks of dormant volcanoes remains lacking. One of the most phenomenal cases is Sinabung Volcano in North Sumatra, Indonesia. After ~400 years of dormancy, the volcano erupted in August and September, 2010 and continued actively erupting lava and pyroclastic deposits until the latest eruption that was reported on May 11th - 17th, 2022 (**Gunawan et al., 2019, Global Volcanism Program, 2022**). This implies that a volcano

that erupted hundreds of years ago, experiencing a quiescence period (with no historic record), can be re-activated and potentially present a threat for the population in the nearby area. Therefore, studying the latest eruption products may provide important insight for understanding the eruption-triggering factors, as well as the present magma reservoir condition (e.g. **Macías et al. 2003; Castro and Dingwell, 2009; Andrews, 2014; Castruccio et al., 2016; Araya et al., 2019**).

Mount Seminung (a post-caldera volcano of Ranau) in South Sumatra, Indonesia (see **Figure 1a**) is not an exception, as most previous research focused on geothermal and structural geology aspects (**Natawidjaja et al., 2017; Maryadi et al., 2022**). Namely, we identified that Seminung Volcano has experienced an explosive phase (unidentified eruption age), as indicated by a ~370 cm-thick sequence of pumice- and scoria-bearing pyroclastic deposits at ~3.8 km northeast distance from the vent, just

Corresponding author: Indranova Suhendro

e-mail address: indranova.suhendro@ugm.ac.id
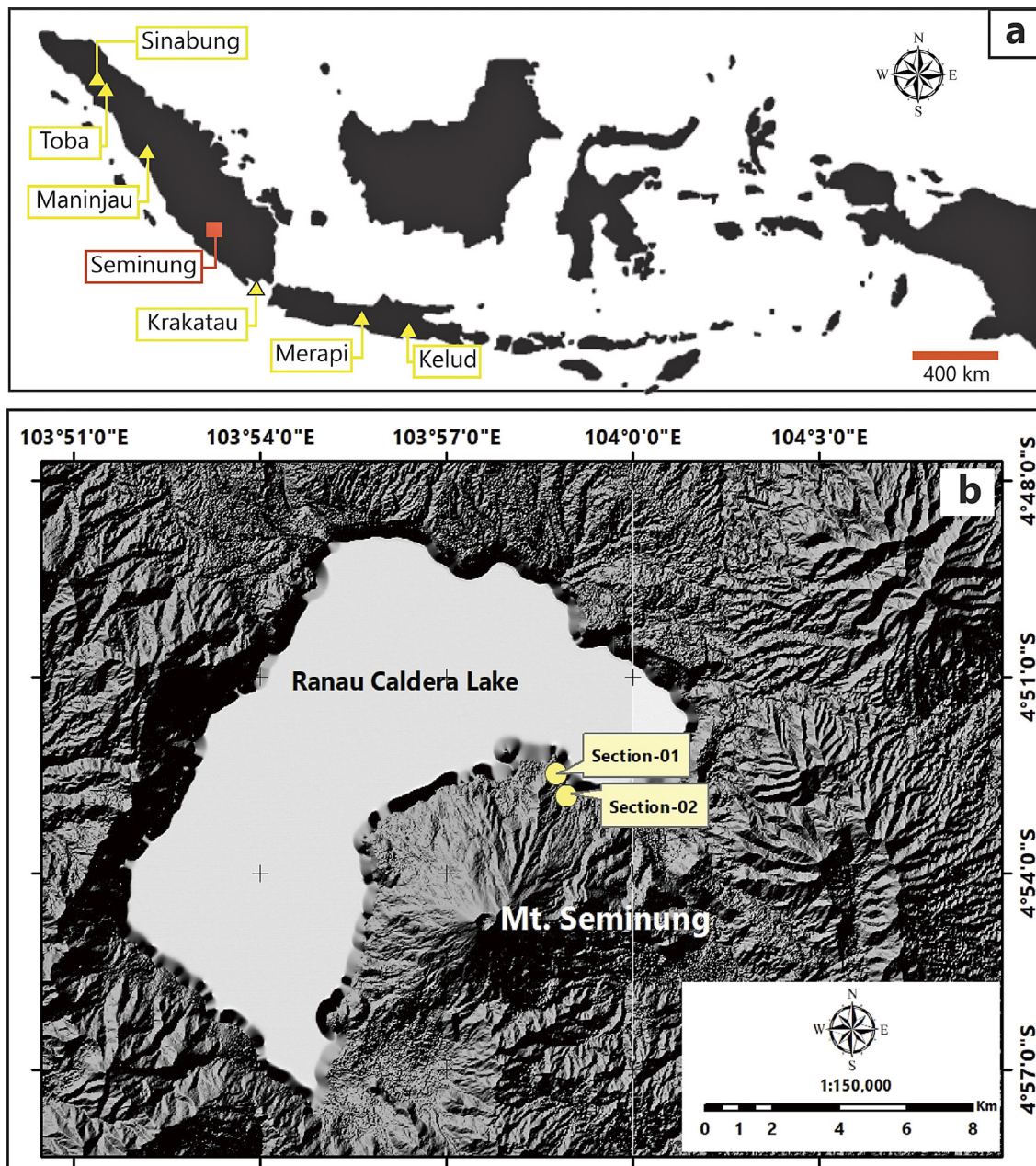
Figure 1: (a) Location of Mount Seminung relative to nearby well-known volcanoes such as Sinabung, Toba, Maninjau, Krakatau, Merapi, and Kelud. (b) Sampling locations of this study are shown by the yellow circles (Section-01 and 02).

below the present soil. This implies that Seminung Volcano has been capable of producing an explosive eruption which might happen again in the future. This is the first study that reports the stratigraphy, componentry, petrography, and geochemical (glass and plagioclase compositions) data of one of the youngest pyroclastic deposits of Seminung Volcano, with the aim to capture the pre-eruptive and present magma reservoir conditions beneath Mount Seminung. In addition, we also evaluate the magma vesiculation history during ascent by quantifying the vesicles preserved in pumice and scoria clasts (**e.g. Toramaru 2006, 2014; Shea, 2017; Suhendro et al., 2022**). This information can be used as basic knowledge to iden-

tify the possible risk caused by the eruption of Mount Seminung, which is important for hazard assessment and minimizing the number of victims.

2. Geology of Seminung Volcano

The Ranau volcanic complex (RVC) in South Sumatra, Indonesia has produced two series of thick ignimbrite deposits, namely units C and B (**Gunawan, 2020**). There has been no report on the occurrence of the older ignimbrite (unit C), while the younger ignimbrite (unit B) corresponds to the product of the ~33.6 ka caldera-forming eruption of Ranau (i.e. Ranau tuff; **Natawidj-**
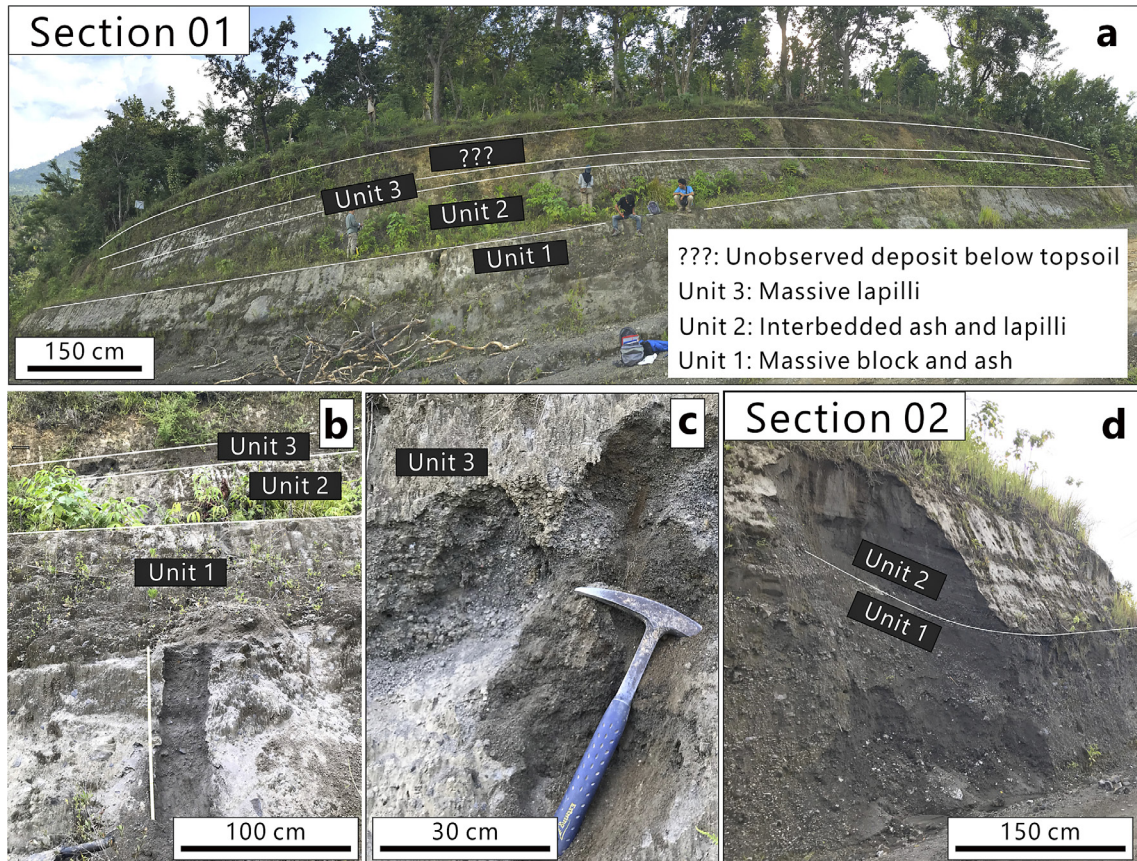
Figure 2: (a, b) Outcrop images at Section 01 showing the occurrence of massive block and ash (unit 1), interbedded ash and lapilli (unit 2), and massive lapilli (unit 3). (c, d) Close-up images of unit 3, and unit 1 and 2, respectively.

adja et al., 2017**). Both ignimbrites displayed nearly identical bulk-rock silica contents (~73.5 wt. % SiO$_2$ for unit C and 72–74 wt.% SiO$_2$ for unit B); however, their petrography and modal mineralogy are different (**Gunawan, 2020**). In particular, unit C is nearly aphyric (0–5 % pheno-crystallinity), and quartz- and biotite-free. Whereas, unit B is typically porphyritic (3–20 % pheno-crystallinity), and includes ubiquitous quartz and biotite phenocrysts. Now, the main activity takes place at Mount Seminung, i.e. the post-caldera volcano of the RVC (**Natawidjadja et al., 2017**). The eruption of Mount Seminung mainly produced lava flows and pyroclastic deposits, with silica contents ranging from 59.2 to 61.8 wt. % (bulk-rock). However, detailed stratigraphic information of these units is unknown, and there is no historical record of any volcanic activity from Mount Seminung.

Noteworthy, Mount Seminung lies on a ~1,650 km long dextral fault (extending from the northernmost towards the southernmost part of Sumatra Island), namely the Great Sumatran Fault, which is formed by the oblique subduction between the Indian and Eurasian plates (**Bellier and Sebrier, 1995; Natawidjadja et al., 2017; Acocella et al., 2018; Dewanto et al., 2022**). Up to the present day, the GSF remains active, with an estimated slip rate of 6.8–26.0 mm/year (**Natawidjadja et al.,**

2017; Acocella et al., 2018). This is dangerous because a small change in strain across a fault zone can initiate the magma ascent (e.g. **Kriswati et al., 2019**).

Recently, Mount Seminung is also known as a geothermal prospect area (up to 30 MW), as indicated by the occurrence of potential reservoir rock, cap rock, geological structures, heat source, and hot springs (**Afiat et al., 2021; Maryadi et al., 2022**). Based on the magnetotelluric study, **Maryadi et al. (2022)** suggest that the heat source of Seminung is expected to be located at a depth greater than 4 km, and might correspond to the present depth of the active magma reservoir.

3. Methods

3.1. Fieldwork and sampling strategy

Mount Seminung is densely populated with vegetation; thus, finding outcrops was challenging. It is also important to mention that the reported lava outcrops by **Westerveld (1952)** were only observed near the summit region (~1400 m elevation above sea level). However, two pyroclastic outcrops were discovered on the northern flank of Seminung, namely sections 01 and 02 (the distance between each outcrop is ~500 m). The location of sections 01 and 02 are shown in **Figure 1b.** Sampling

of each unit (see detailed explanation in section 4.1.) was performed in section 01 (see **Figure 2a, b, c**) because it provides a more complete stratigraphic section than in section 02 (see **Figure 2d**). Subsequently, the collected samples were used for laboratory analyses, including grain size distribution (GSD), componentry, petrography, chemical (glass and mineral compositions), and textural (vesicles) studies.

3.2 Grain size distribution and component analysis

Manual sieving prevents the samples from experiencing further erosion which may add to the weight of grains at the finest size intervals and cause an overestimation of the grain size distribution (**Walker and Croasdale, 1971**). Thus, our samples were manually separated using a set of dry-sieving tools with one-phi interval spacing, ranging from -5ϕ (>32 mm) to 4ϕ (<1/16 mm).

Next, we manually observed and counted the observed clasts to identify the componentry. The component analysis was performed on -5ϕ to -2ϕ sieves (32 − 4 mm). Based on the qualitative traits, we classified the components as follows: grey pumice (GP), brown pumice (BP), scoria (SC), banded (between pumice and scoria), lithics (mainly volcanic), and accretionary lapilli (AL) (see **Figure 4**). Hereafter, componentry data are reported as a number fraction (i.e. total number of each component type is divided by total number of counted grains), where C_{GP}, C_{BP}, C_{SC}, C_{banded}, C_{lithic}, and C_{acc} represent the componentry of grey pumice, brown pumice, scoria, banded pumice, lithics, and accretionary lapilli, respectively.

3.3. Petrography, quantifying phenocryst and vesicles

A total of 17 thin sections (including grey pumice, brown pumice, and scoria) from three distinct layers were analyzed using a polarized microscope at the Petrology and Volcanology Laboratory, Kyushu University to identify the mineral assemblages and mineral textures (i.e. zoning, sieves). To observe the whole vesicle and crystal textures of each thin section, a mosaic image (SEM images of 30x magnification combined to create a whole image of a sample) was made by a HITACHI TN3030 Plus Miniscope SEM at the Petrology and Volcanology Laboratory, Kyushu University.

Crystals larger than 0.1 mm (phenocryst; **Noguchi et al. 2008a**), and vesicles larger and smaller than 0.1 mm (pheno-vesicle and matrix-vesicle; **Suhendro et al. 2022**) were manually digitized using Corel Draw X7, and processed by image-J software to obtain textural parameters such as frequency (number), diameter, and area. A mosaic image was used for tracing phenocryst and pheno-vesicle, as it is capable of depicting the largest and smallest size of phenocrysts and pheno-vesicles, while the 500× magnification was used for its capability

to capture the largest and smallest matrix-vesicle size. The coalesced vesicles (both for pheno- and matrix-vesicles) were manually corrected (i.e. 'decoalesced'), adapting the rules described in **Klug and Cashman (1994, 1996)**.

Textural parameters derived from ImageJ were used to calculate the bulk vesicularity (ϕBV), pheno-crystallinity (ϕPC), pheno-vesicle number density (PVND), and matrix-vesicle number density (MVND). All of the notations and equations refer to **Suhendro et al. (2022)**. In particular, pheno-crystallinity (ϕPC) corresponds to the total area of phenocrysts divided by the total clast area (including vesicle). Meanwhile, pheno-vesicularity (ϕPV) is the ratio of the total pheno-vesicle area to its total clast area (including phenocryst). The matrix fraction from mosaic image (ϕM) needs to be corrected (fMV) using the matrix vesicularity (ϕ_{mv}) from higher magnifications (i.e. 500x) to include the smallest size of the matrix vesicle, as shown in **Equations 1** and **2**:

$$\phi MV = \phi_{mv} \times \phi M \qquad (1)$$

$$\phi M = 1 - \phi PC - \phi PV \qquad (2)$$

using corrected matrix vesicularity (ϕMV), bulk vesicularity (ϕBV) is calculated, as shown in **Equation 3**:

$$\phi BV = \phi PV + \phi MV \qquad (3)$$

Crystallinity should show the impression of crystal phase-only on juvenile materials, hence the total area of the ϕPC calculation needs to be corrected by bulk vesicularity following this equation:

$$\phi° PC = \phi PC / (1 - \phi BV) \qquad (4)$$

Furthermore, the reported PVND and MVND (under the homogeneity assumption; **Suhendro et al., 2022)** was obtained from the following equations:

$$PVND\left(N_{vp}\right) = \left(\frac{N_{ap}}{D_p}\right) / \left(1 - \phi_{BV}^{*}\right) \qquad (5)$$

$$VND = \left(\frac{N_{am}}{D_m}\right) / \left(1 - \phi_{mv}\right) \qquad (6)$$

where N_{ap}, N_{am}, D_p, D_m are the number of pheno-vesicles per unit area, matrix-vesicles per unit matrix area, the average diameter of pheno- and matrix-vesicles, respectively. In addition, ϕ_{BV}^{*} is the phenocryst-free bulk vesicularity.

3.4. Glass and mineral composition

Glass and mineral (i.e. plagioclase and biotite) chemical compositions were obtained by a field emission electron microprobe analysis (FE-EPMA) at the Faculty of Science, Kyushu University, Japan. The accelerating voltage was set at 15 kV with a beam size of 3 μm in diameter. Core and rim compositions of plagioclase

were measured, while biotite is only represented by the core composition. However, because scoria is biotite-free, biotite composition is limited to the grey and brown pumice samples. The chemical compositions of plagioclase and biotite are presented in the supplementary material 1.

4. Results

4.1. Field geology

Three main stratigraphic units were observed as follows: (1) massive blok and ash, (2) interbedded ash and lapilli, and (3) massive lapilli. All of these units were observed in section 01, while section 02 lacks the third unit (massive lapilli) (see **Figures 2a and 3a**). Another pyroclastic deposit was also observed above the third unit (or below the present soil); however, it was impossible to perform sampling and detailed observation for this unit because it is located in the uppermost elevation (higher than 3 m), just below the topsoil.

Unit 1 is typically thick (100 and 150 cm at section 01 and 02, respectively), rich in blocky and ash materials with no internal structure (i.e. massive). Unit 2 has a relatively similar thickness to that of unit 1 (up to 150 cm), and is characterized by the intercalation of ash and lapilli layers. Lapilli layers are massive, dominated by ~5 mm clast size, and have thicknesses varying from 5 to 10 cm. While ash layers are typically fine (<1/16 mm) and 10 to 45 cm thick, with the uppermost layer showing normally graded structure. Unit 3 is significantly thinner (50 cm) and predominantly consists of lapilli with a massive structure.

4.2. Depositional mechanisms

Based on the median and sortation plot, unit 1 is identified as a pyroclastic density current (PDC) deposit, as characterized by the bimodal grain size distribution with predominantly ash-sized materials (Md = 0.9 mm) (e.g. **Jones, et al., 2023**) (see **Figures 3** and **4**). The remaining units are defined as pyroclastic fall deposits; however, unit 2 exhibits distinctive grain size variation than that of unit 3 (see **Figure 3**). In particular, unit 2 is normally skewed and rich in ash-sized particles (Md = 0.6 mm), while unit 3 is positively skewed and rich in lapilli (Md = 3.8 mm) (see **Figure 3**).

4.3. Summary of componentry

Our observation suggests that all stratigraphic units include brown pumice (BP), grey pumice (GP), and sco-
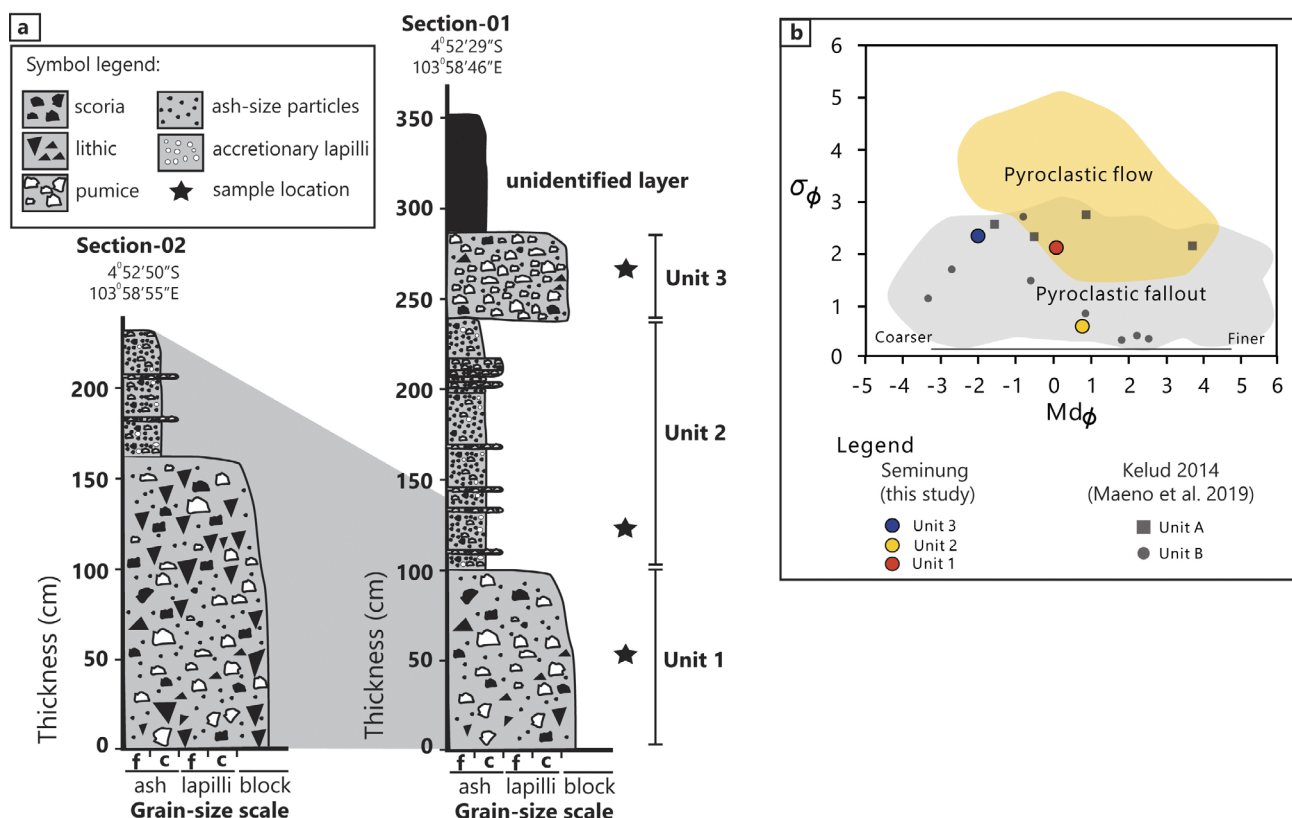
Figure 3: (a) Stratigraphic column of the youngest pyroclastic deposits of Mount Seminung. The star symbol denotes the sampling location. Note that unit 2 is typically dominated by ash; hence, sampling was performed at one of the most representative ash layers for further laboratory analyses. Correlation between Section-01 and Section-02 deposits are based on their similar characteristics and located at a close distance. (b) The plot between sortation vs median diameter (after **Walker 1971**) categorizes unit 1 as pyroclastic flow (herein, referred as pyroclastic density currents) and the remaining unit (Unit 2-3) as pyroclastic fall deposits.
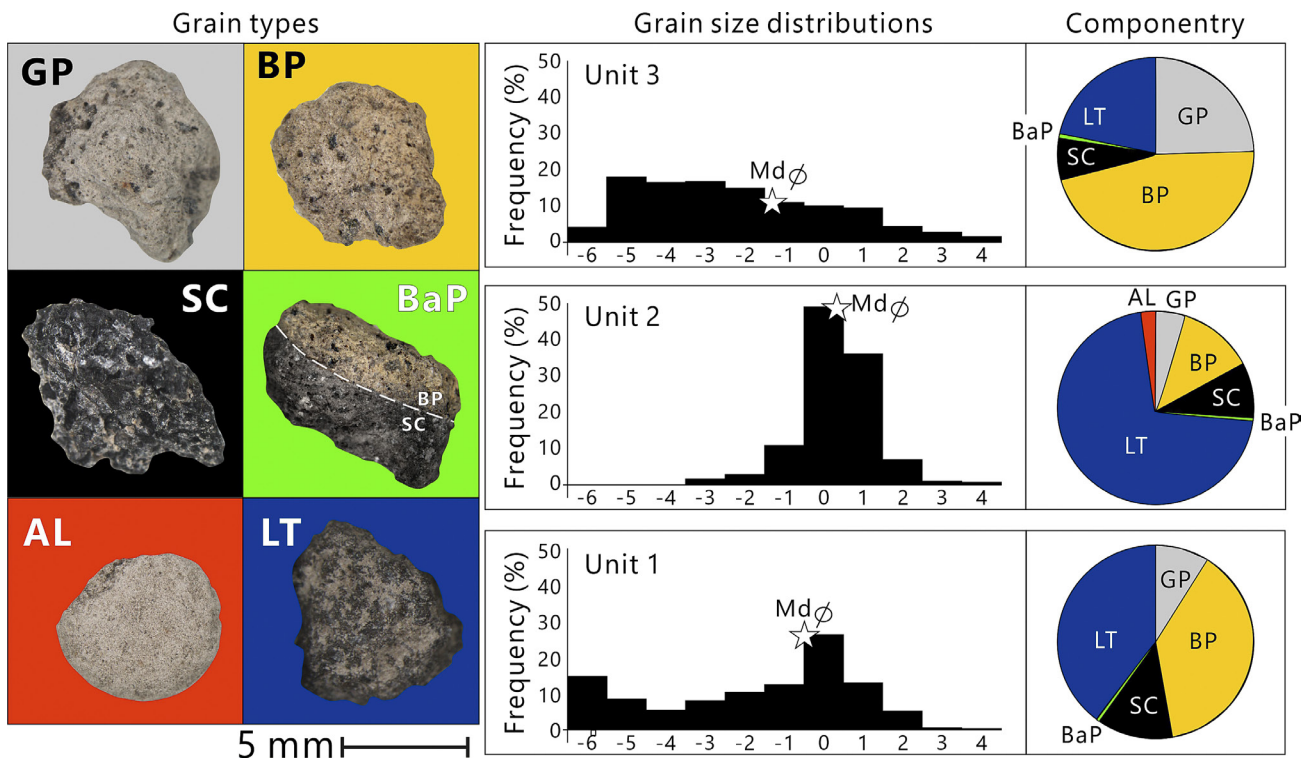
Figure 4: Histogram of the grain size distribution shows the unimodal distribution for fallout deposits (unit 2 and 3) and bimodal distribution for PDC (unit 1). Each color in pie diagrams represents the abundance of each component from each unit. GP, grey pumice; BP, brown pumice; SC, scoria; AL, accretionary lapilli; BaP, Banded pumice; LT, lithic.

Table 1: Componentry result of Seminung pyroclastic deposits. n represents the number of each component type in each unit, is the total number of counted grains, and *C* is the number fraction (n /).

Unit (Observed grain size)	Juvenile; n ($C_{GP/BP/SC}$)			Banded pumice; n (C_{banded})	Accretionary lapilli; n ($C_{acc.}$)	Lithics; n (C_{lithic})	Total number of clasts (n_{tot})
	Grey pumice (GP)	Brown pumice (BP)	Scoria (SC)				
Unit 3	138 (16.2)	259 (30.5)	18 (2.2)	7 (0.8)	0 (0)	428 (50.3)	850
Unit 2	20 (3.7)	44 (8.2)	29 (5.4)	2 (0.4)	4 (0.8)	435 (81.5)	534
Unit 1	91 (17.2)	195 (37.0)	29 (5.4)	2 (0.4)	0 (0)	211 (40.0)	528

ria (SC) as the main juvenile phases, with banded pumice as a minor juvenile component. The non-juvenile (lithics) component is represented by porphyritic lava. In addition, only unit 2 contains a small number of accretionary lapilli (AL). The representative image of each component is shown in **Figure 4**.

Among all juvenile clasts, brown pumice occurs as the most dominant phase, followed by grey pumice, scoria, and banded pumice (see **Figure 4**). In particular, unit 1 and 3 exhibit higher content of brown pumice (37.0 and 30.5% C_{BP}, respectively), grey pumice (17.2% and 16.2% C_{GP}, respectively) and scoria (5.4 and 2.2 % C_{SC}, respectively), than that of unit 2 (8.2, 3.7, and 5.4% for brown pumice, grey pumice, and scoria, respectively). All units contain a small amount of banded pumice, var-

ying from 0.4 to 0.8%. The representative componentry data is listed in **Table 1**. Lithic (non-juvenile; cognate) materials mainly correspond to dark grey and black porphyritic lava without and/or low vesicle populations. The highest lithics portion is observed in unit 2 (C_{lithic} = 81.5%), followed by unit 3 and unit 1 (50.3 and 40% C_{lithic}, respectively) (see **Table 1**).

4.4. Petrography, and glass and mineral compositions

The representative petrographic images and the mineralogical variation of each juvenile clast are shown in **Figures 5** and **6b**. Brown pumice is poorly to moderately vesicular and phenocryst-rich. Phenocrysts in the
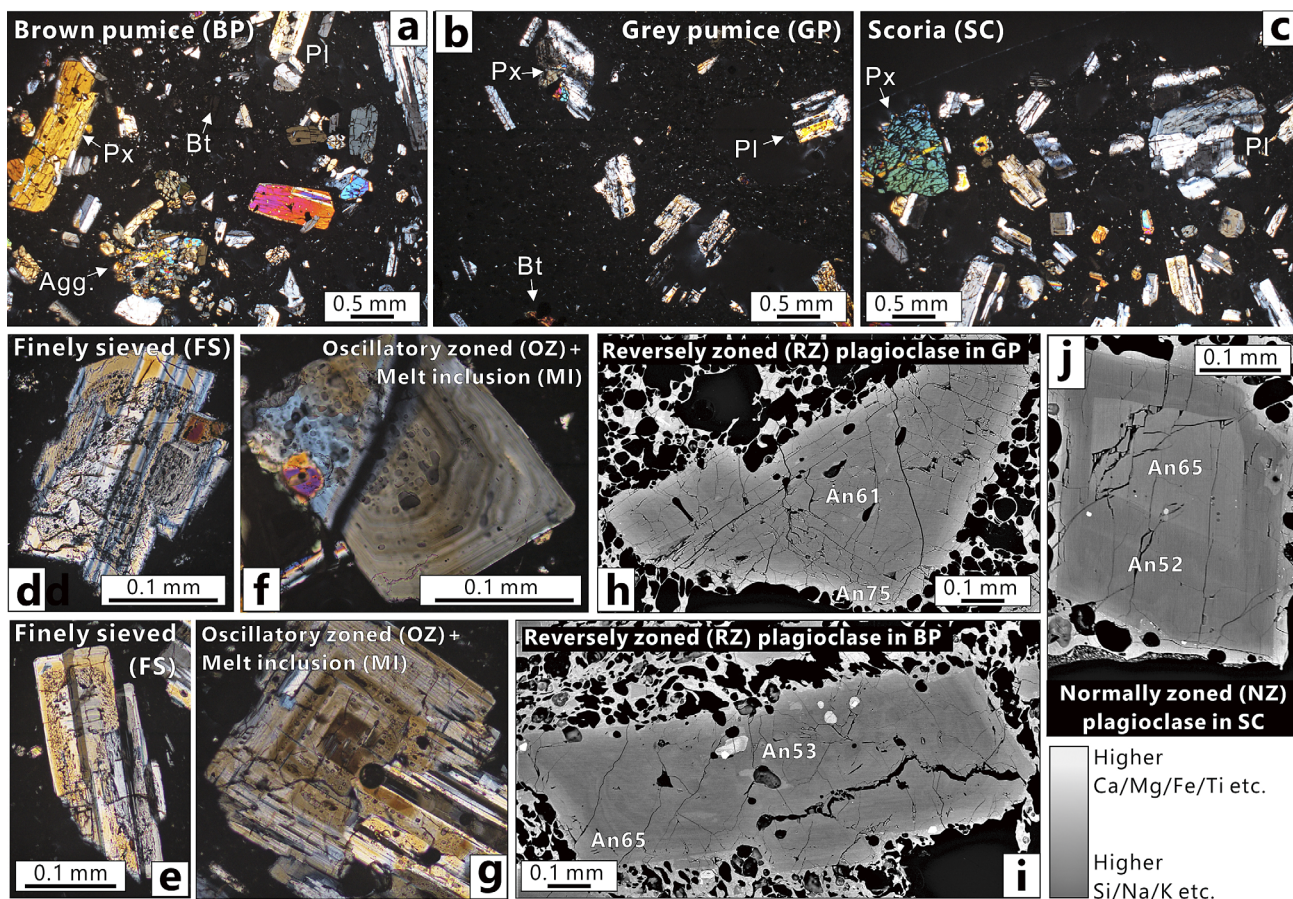
Figure 5: (a, b, c) Representative petrographic image of brown pumice, grey pumice, and scoria, respectively. Plagioclase in grey and brown pumice often exhibit finely-sieved (d, e), oscillatory zoned with melt inclusions (f, g) and reversely zoned (h, i) textures. Noteworthy, most of plagioclase in scoria is normally zoned (j).

Table 2: Glass compositions of grey and brown pumice, and scoria. All elements are shown in weight percent (wt. %) and are normalized to 100 (volatile-free).

Unit		SiO_2	TiO_2	Al_2O_3	FeO	MnO	MgO	CaO	K_2O	Na_2O	Total
Unit 3	GP (n=8)	72.23	0.69	14.19	3.36	0.09	0.69	2.20	3.11	2.28	100.00
	BP (n=8)	68.16	0.76	15.21	5.03	0.12	1.34	3.42	2.68	2.72	100.00
	SC (n=8)	65.42	1.16	17.19	4.17	0.09	2.29	3.38	2.05	4.25	100.00
Unit 2	GP (n=8)	71.48	0.73	14.77	3.29	0.07	0.73	2.13	3.16	2.19	100.00
	BP (n=8)	67.69	0.53	15.42	5.13	0.11	1.29	3.39	2.58	3.31	100.00
	SC (n=10)	65.05	1.19	17.05	4.22	0.09	2.37	3.40	2.10	4.38	100.00
Unit 1	GP (n=12)	72.98	0.64	14.64	2.68	0.11	0.52	1.98	2.84	2.28	100.00
	BP (n=15)	69.44	0.36	14.36	5.00	0.11	1.43	2.67	2.78	3.25	100.00
	SC (n=10)	66.45	0.83	16.42	4.00	0.09	2.16	3.19	2.39	3.25	100.00
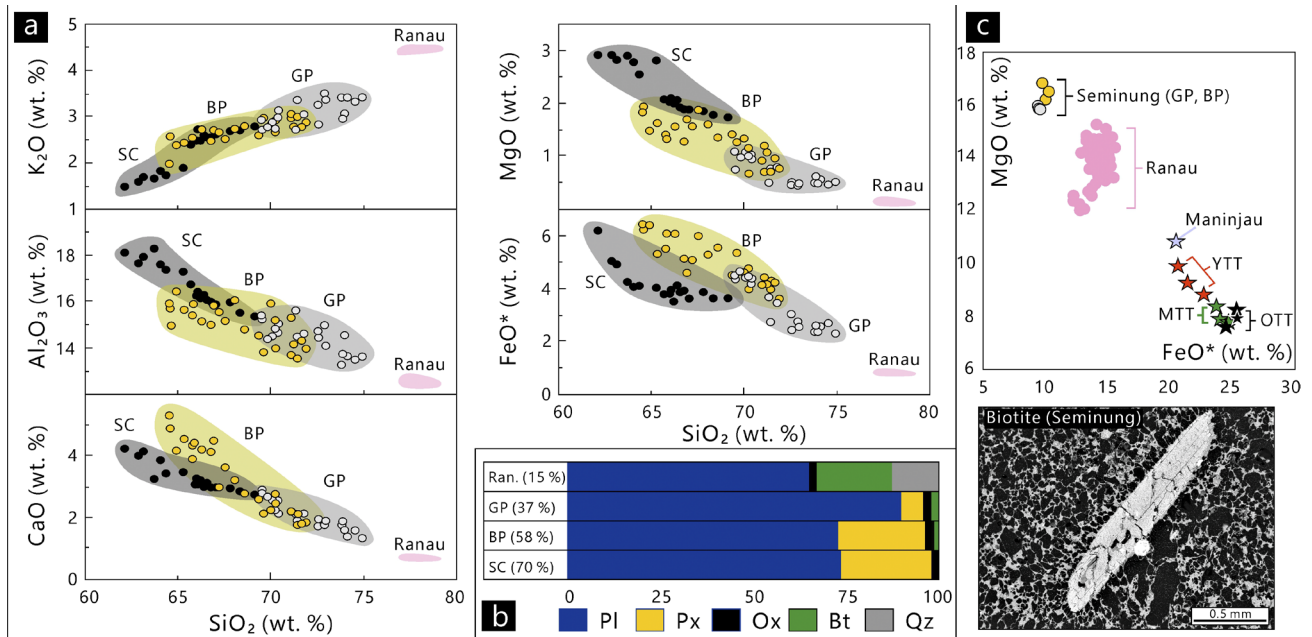
Figure 6: (a-c) Glass composition, modal mineralogy, and biotite composition of juveniles from Seminung and Ranau caldera (**Natawidjadja et al. 2017; Gunawan 2020**). (a) Glasscompositions of scoria (black circle), brown pumice (yellow circle), and grey pumice (white circle) shows distinct pattern to Ranau pumice. (b) Pumice is typically biotite-bearing, while scoria is biotite-free. Pl, Px, Ox, Bt, and Qz refer to plagioclase, pyroxene, oxide minerals, biotite, and quartz, respectively.). (c) Comparison of biotite compositions from Seminung and Sumatran calderas (Ranau, Maninjau, and Toba). Abbreviations: SC, scoria; BP, brown pumice; GP, grey pumice.
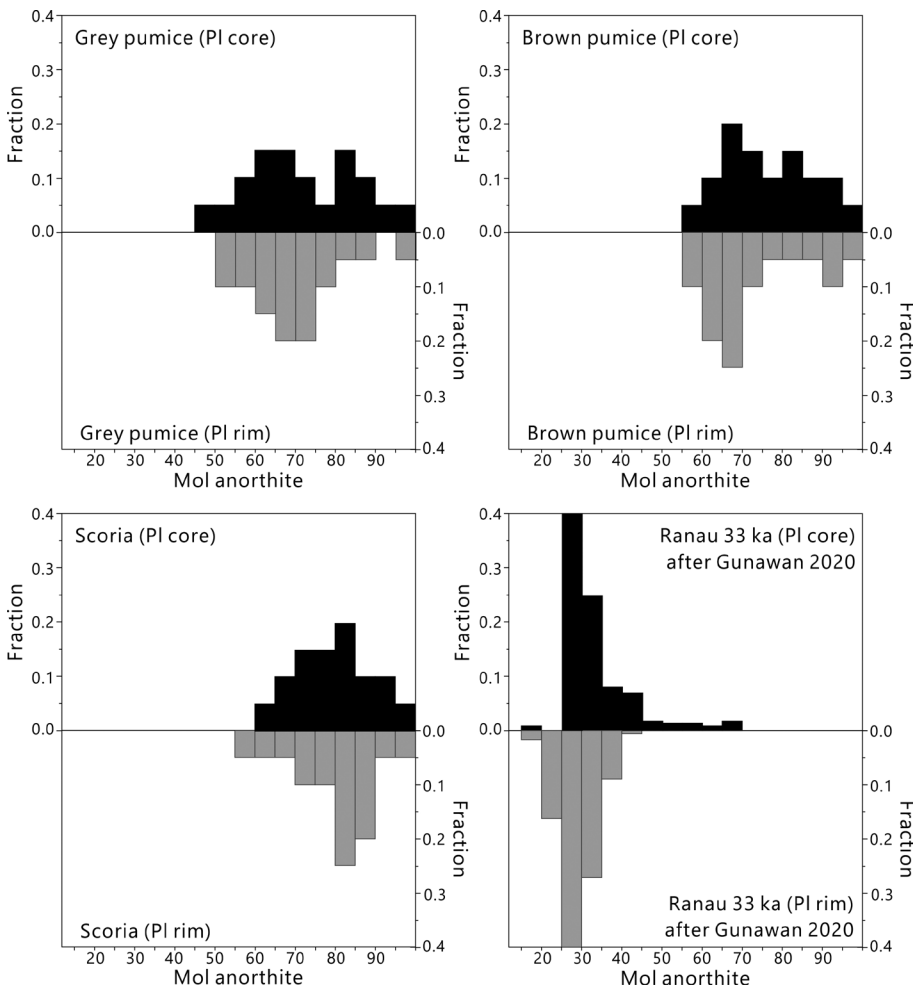
Figure 7: Histograms showing core and rim anorthite number (#An) of plagioclase phenocryst for each juvenile type from Mount Seminung compared with pumice from Ranau 33 ka (**after Gunawan, 2020**). Note the bimodality of anorthite contents in both pumice types, which is not observed in scoria.
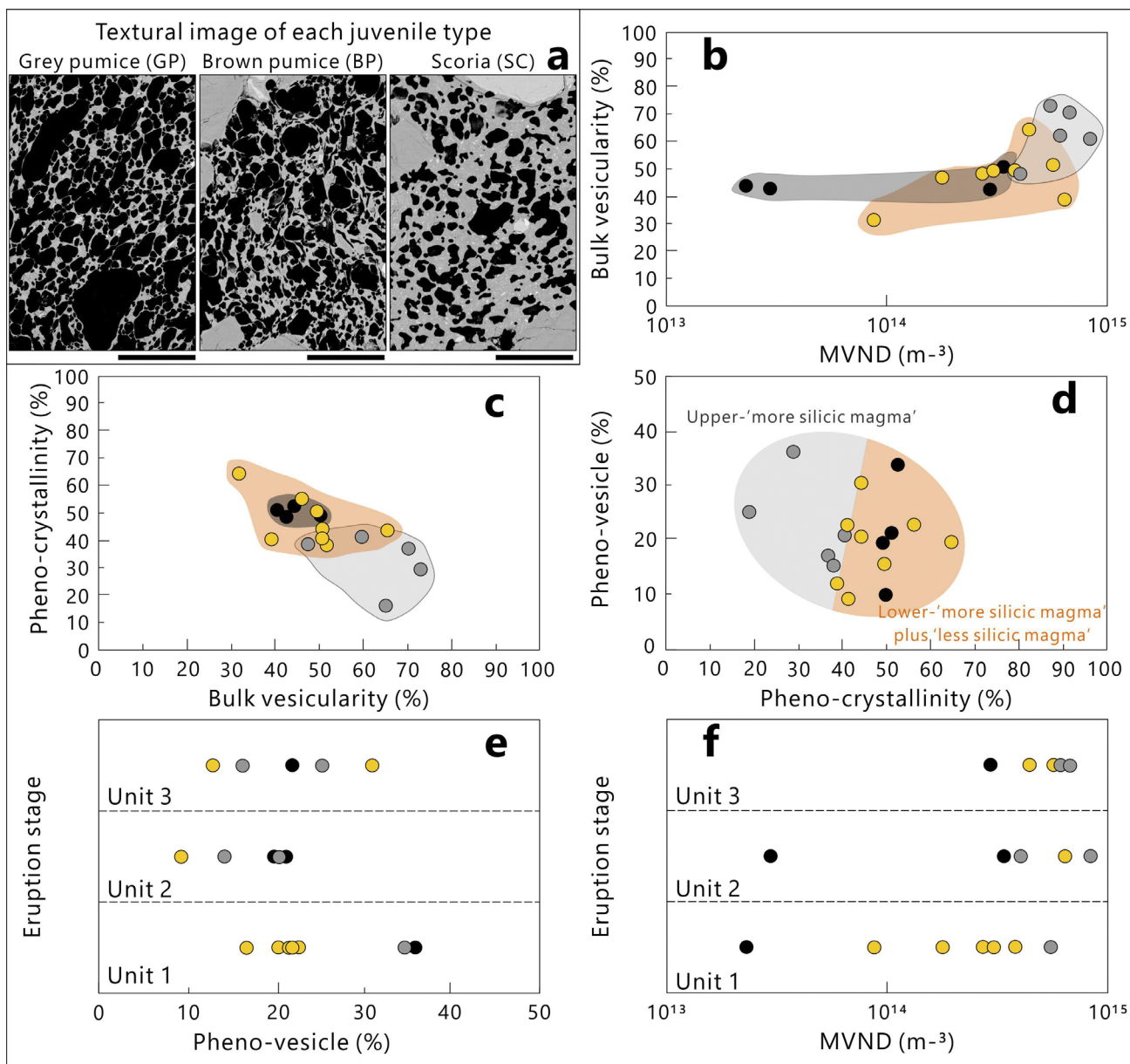
Figure 8: Correlation of textural data from scoria (black circle), brown pumice (yellow circle), and grey pumice (grey circle). (a) Textural BSE image of each juvenile type (black bar scale = 0.25 mm). (b) Bulk vesicularity compared with matrix-vesicle number density (MVND) shows a slightly positive correlation. (c, d) Bulk-vesicularity and pheno-vesicularity are negatively correlated with pheno-crystallinity. (e, f) As pheno-bubble decrease, the intensity of matrix-bubble nucleation increases.

brown pumice are presented by plagioclase, pyroxene, biotite, and oxides (see **Figure 5a**). Grey pumice is moderately to highly vesicular and has a relatively lower phenocryst content than brown pumice (see **Figure 5b**). Note that phenocryst types in grey pumice are similar to that of brown pumice. Scoria (see **Figure 5c**) exhibits low to moderate vesicularity and includes abundant phenocryst of plagioclase, pyroxene, and oxides (biotite-free). Most of the plagioclase phenocrysts in grey and brown pumice are reversely zoned and finely sieved with abundant fractures and honeycomb texture (see **Figure 5d-i**). Such textures were absent in scoria; most plagioclase displayed normally zoned texture with minor fractures (see **Figure 5j**). Noteworthy, plagioclase is

also rich in channel-shaped melt inclusions (see **Figure 5f, g**).

Grey pumice represents the most evolved (69.5–74.9 wt. %) juvenile phase, followed by brown pumice and scoria (64.5–71.5 and 62.1–69.2 wt. % , respectively) (see **Figure 6a**). SiO_2 is positively correlated with K_2O, but showing negative correlation with Al_2O_3, CaO, MgO, and FeO*. Noteworthy, scoria has a trend that is not linear with grey and brown pumices. The representative glass compositions are shown in **Table 2**.

Pumice (grey and brown) and scoria exhibit distinctive variations in mineral assemblages (see **Figure 6**). Brown and grey pumice are mineralogically similar (plagioclase, pyroxene, biotite, and oxides; biotite-bear-

Table 3: Textural parameters of grey, brown pumices, and scoria.

Unit	Juvenile type	φ_{BV}	Pheno-vesicle			Matrix-vesicle			φ_{PC}
			(mm)	φ_{PV}	(m^{-3})	(mm)	φ_{MV}	(m^{-3})	
Unit 3	GP	0.70	0.18	0.17	8.2x10^{10}	0.009	0.53	6.9x10^{14}	0.37
	GP	0.64	0.15	0.25	8.2x10^{10}	0.010	0.38	6.2x10^{14}	0.19
	BP	0.65	0.22	0.31	8.8x10^{10}	0.013	0.34	4.5x10^{14}	0.44
	BP	0.51	0.21	0.12	3.0x10^{10}	0.013	0.39	5.8x10^{14}	0.39
	SC	0.41	0.19	0.22	4.9x10^{10}	0.011	0.19	3.0x10^{14}	0.51
Unit 2	GP	0.60	0.17	0.20	9.7x10^{10}	0.012	0.40	8.5x10^{14}	0.41
	GP	0.48	0.17	0.15	6.6x10^{10}	0.013	0.35	4.0x10^{14}	0.38
	BP	0.39	0.19	0.09	4.0x10^{10}	0.010	0.30	6.5x10^{14}	0.41
	SC	0.43	0.18	0.19	1.9x10^{11}	0.028	0.24	3.0x10^{13}	0.49
	SC	0.50	0.17	0.19	8.4x10^{10}	0.015	0.31	3.4x10^{14}	0.49
Unit 1	GP	0.73	0.20	0.36	1.7x10^{11}	0.014	0.37	5.6x10^{14}	0.29
	BP	0.50	0.22	0.23	4.0x10^{10}	0.016	0.27	3.2x10^{14}	0.41
	BP	0.50	0.21	0.16	3.8x10^{10}	0.014	0.34	3.8x10^{14}	0.50
	BP	0.32	0.20	0.20	4.5x10^{10}	0.015	0.12	8.8x10^{13}	0.65
	BP	0.46	0.17	0.23	8.7x10^{10}	0.018	0.23	1.8x10^{14}	0.56
	BP	0.50	0.22	0.21	3.9x10^{10}	0.015	0.29	2.8x10^{14}	0.44
	SC	0.44	0.20	0.40	1.1x10^{11}	0.019	0.06	2.3x10^{13}	0.52

ing), but the relative abundance for each phase (especially for plagioclase and pyroxene) is significantly different. In particular, the average modal of plagioclase, pyroxene, biotite, and oxides in brown pumice are 73 vol.%, 20 vol.%, 5 vol.%, and 2 vol.%, respectively. Grey pumice contains the highest plagioclase content (87 vol.%), followed by pyroxene, oxide, and biotite (7 vol.%, 2 vol.%, and 4 vol.%, respectively). In contrast, scoria has no biotite, with plagioclase being the most dominant phase (74 vol.%), followed by pyroxene (21 vol.%) and oxides (5 vol.%). These results are remarkably different compared with pumices from Ranau caldera, which has a high content of biotite (18 vol.%) and quartz (12 vol.%) (**Gunawan, 2020**). In addition, biotite mineral compositions of brown and grey pumice are distinctive to the other biotite from Sumatran calderas such as Ranau, Maninjau, and Toba (**Figure 4c; Natawidjaja et al., 2017**).

Anorthite number (An) of plagioclase exhibits distinctive patterns between pumice and scoria (see **Figure 7**). In particular, brown pumice and grey pumice are characterized by a bimodal distribution of An#, whereas scoria shows unimodal patterns. Grey pumice includes a relatively more evolved plagioclase than those of brown pumice and scoria. In particular, the core and rim compositions of plagioclase in grey pumice is An$_{45.1-95.3}$ and An$_{52.1-95.5}$, respectively. For brown pumice, the anorthite core and rim compositions is An$_{57.9-97.3}$ and An$_{59.1-97.6}$ respectively. While the core and rim compositions of plagioclase in scoria are An$_{63.4-97.1}$ and An$_{59.8-96.6}$, respectively.

4.5. Mineral texture, and glass and mineral compositions

The bulk vesicularity (fBV) of all juvenile materials is positively correlated with matrix-vesicle number density (MVND) and negatively correlated with pheno-crystallinity (fPC) (see **Figures 8a, b**). Grey pumice is found to be the most vesicular (0.48–0.73 fBV, 0.15–0.36 fPV, 3.0×10^{14}–8.5×10^{14}m^{-3} MVND) and the least crystalline (0.19–0.41 fPC) juvenile clasts. Brown pumice shows lower vesicularity and higher crystallinity than grey pumice (0.32–0.65 fBV, 0.09–0.31 fPV, 0.9×10^{14}–6.5×10^{14}m^{-3} MVND, and 0.39–0.65 fPC). While scoria is characterized by the narrow variation of low vesicularity and high crystallinity values (0.41–0.50 fBV, 0.10–0.36 fPV, 0.2×10^{14}–3.4×10^{14}m^{-3} MVND, and 0.49–0.52 fPC (see **Figure 8c**). It is also found that pheno-vesicle fraction and matrix-vesicle number density systematically decrease towards the top of the deposits (see **Figure 8d-f**).

5. Discussion

5.1. Eruption type

Eruption type is generally determined by the existing scheme and model comparing the area of dispersal and degree of fragmentation (**Walker, 1973**), using maximum clast dispersal data and maximum column height of pyroclastic fall deposits (**Carey and Sparks, 1986**), and/or considering the thinning rate of tephra fall deposit and grain size parameters (**Pyle, 1989; Bonadon-**

na and Costa, 2013). These theories require isopach and isopleth maps constructed from many outcrop locations; however, it does not apply to our study because the number of outcrops is limited. Therefore, the eruption type was determined by considering the other parameters, i.e. (1) deposit characteristics (i.e. stratigraphy), and (2) deposit thickness of tephra falls at a certain distance from the vent.

5.1.1. Evidence from the deposit characteristics

Hawaiian and Strombolian eruptions are characterized by the low explosivity behavior; hence, the products mainly consist of lava flows and/or scoriaeous blocks (**e.g. Sigurdsson 2000; Castro and Feisel 2022; Lamb et al. 2022**). A low magma viscosity with low SiO_2 content is therefore needed to facilitate these kinds of eruptive styles (i.e. Hawaiian and Strombolian); however, it is unlikely for this case because the erupted juveniles are considerably evolved and viscous, as indicated by the andesitic to rhyolitic glass compositions (see **Figure 6a**). Therefore, the possibility of Hawaiian and Strombolian eruption styles was excluded for the studied deposits.

Vulcanian eruptions are characterized by discrete or pulsatory explosions that mainly produce ballistic blocks, with lithic materials as the most dominant component andubiquitous obsidian (**e.g. Sigurdsson 2000; Alfano et al. 2011, 2012; Trafton and Giachetti 2022; Maeno et al. 2023**). Units 1 and 3 are typically dominated by lapilli, rich in juvenile, and obsidian-free (see **Figures 3** and **4**), thus strongly eliminating the possibility of a Vulcanian eruption style. It is more difficult to interpret the eruptive mechanism of unit 2 because lithic materials occur as the most dominant component; however, the absence of ballistic blocks and obsidian, makes Vulcanian eruption the least plausible option. Nevertheless, further examination is required to determine the eruptive mechanism of unit 2 because the presence of accretionary lapilli may either suggest direct contact between external water with magma (i.e. phreatomagmatic eruption) or rainfall-induced agglutination (**Sigurdsson, 2000**).

Sub-Plinian and Plinian eruptions are very explosive and require the condition of volatile-rich and high-viscosity magmas; this is the reason why most of this eruption style occurred in silicic systems (**Sigurdsson, 2000**). Although products from sub-Plinian and Plinian eruptions are generally vesicular (>0.4 fBV; **e.g. Martel et al. 2021**), juveniles from Plinian eruptions tend to have a higher vesicularity than those of sub-Plinian eruptions. Moreover, Plinian eruptions usually include a relatively lower proportion of lithics (<25 vol.%; **e.g. Walker et al., 1984; Sable et al., 2006; Constantini et al., 2009**) than sub-Plinian eruptions (up to 50 vol.%; **e.g. Alfano et al., 2011, 2012; Castruccio et al., 2016; Muller et al., 2022; Suhendro et al. 2023**). This characteristic, coupled with the fact that the studied deposits

are evolved (63.1–74.9 wt.% ; see **Figure 4a**), vesicular (0.3–0.7 fBV; see **Figure 8a**), and have abundant lithics (>40% ; see **Table 1**) suggest that the youngest pyroclastic deposits of Seminung may have originated from sub-Plinian instead of Plinian eruptions.

In addition, many studies have reported that sub-Plinian eruptions were initiated by an opening phase that produces lithic-rich deposits and followed by pumice and/or scoria-bearing lapilli fallout deposits with occasional lithic fragments as the main phase, and alternating layers of lapilli-ash deposits. For example, the Ho-I, Ho-II, Ho-III groups of the Hoei eruption (A.D. 1707) from Fuji (**Miyaji et al., 2011**), the layer α, layer β, layer χ-υ of the May, 2008, Chaitén eruption (**Alfano et al., 2012**), the Unit T1, Unit T2 (without initial phase) of the 1914 Taisho eruption of Sakurajima (**Todde et al., 2017**), and the deposits from the A.D. 472 eruption of the Somma Volcano (**Rolandi et al., 2004**). Our stratigraphy (see **Figures 2** and **3a**) shows a similar pattern to those of the reported sub-Plinian eruptions, thus supporting our idea that the eruption reached magmatic-sub-Plinian intensity.

5.1.2. Evidence from deposit thickness

In this section, the thickness of the magmatic-origin of the pyroclastic fall deposit (unit 3) is compared with the others to justify our argument in the previous section using main and orthogonal dispersal axis of the established isopach maps. In our case, unit 3 (i.e. massive lapilli fall) is 50 cm thick, and is located at ~3.8 km from the vent. Under the assumption of exponential thinning of tephra falls (**Tajima et al. 2013**), it is likely that a similar eruption scale tends to have a similar deposit thickness and grain size at a certain distance from the vent. In general, lapilli fallout deposits discharged from Sub-Plinian eruption at 3-4 km from the vent has a thickness of less than 100 cm (major axis) and 60 cm (minor axis); for example, unit La of the A.D. 472 eruption from Somma Volcano (**Rolandi et al., 2004**); Unit C of the Hoei eruption (A.D. 1707) from Fuji (**Miyaji et al., 2011**); Unit T1 of the 1914 Taisho eruption of Sakurajima (**Todde et al., 2017**). While lapilli fallout deposits generated from Plinian eruptions (at 3-4 km distance from the vent) are significantly thicker, ranging from 98-300 cm and 60-110 cm for major and minor axis, respectively (e.g. the scoria fall of 122 B.C. from Etna Volcano (**Coltelli et al., 1998**); scoria fall of Tarawera 1886 (**Walker et al., 1984**); white pumice Plinian fallout by Popocatépetl Volcano in Central Mexico (**Siebe et al., 2017**). Moreover, the present crater diameter of Seminung Volcano is considerably big, reaching ~600 m. Noteworthy, this crater size is identical to the aforementioned Somma Volcano (Vesuvius; which generated the A.D. 472 Sub-Plinian eruption), yet relatively small compared to the typical Plinian eruptions (>1 km crater diameter), such as the 2014 eruption of Kelud (**Maeno et al., 2019**). Thus, it is likely that the studied deposits are more comparable to those of sub-Plinian eruptions rather than Plinian eruptions.
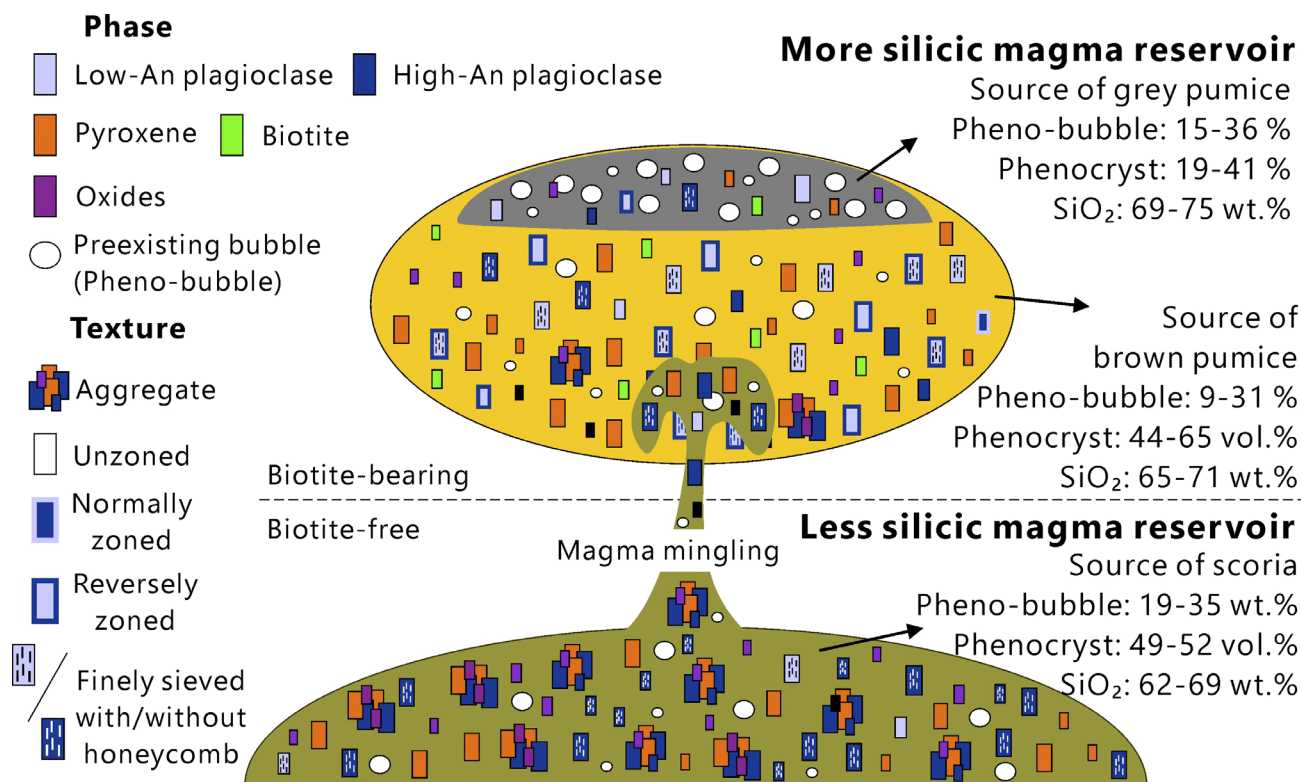
Figure 9: Pre-eruptive magma reservoirs condition of Mount Seminung. Note that the shallow more silicic magma reservoir experienced stratification of melt, pheno-bubble, and phenocryst. While the deeper less silicic magma reservoir does not exhibit the characteristics of magma stratification.

5.2. Mt. Seminung magmatic system

Grey and brown pumice show linear compositional trends, with grey pumice being more evolved than brown pumice. Such a linear correlation suggests a co-magmatic origin which means both pumice types originated from the same magma chamber (see **Figure 6a** and **Figure 7**) (**Ginibre et al., 2004, Kaneko et al., 2007, Forni et al., 2016, Suhendro et al., 2021**). This is supported by the fact that both grey and brown pumice include biotite as the main phenocryst phases (see **Figure 6b**). In contrast, scoria exhibits a compositional pattern that is non-linear to the pumice trend and distinctive mineralogy (biotite-free) to those of grey and brown pumices (see **Figure 6b**). This suggests that scoria formed from a different magma reservoir with different crystallization histories (hereafter, the more silicic and less silicic magma terms are used to define the origins of grey-brown pumice and scoria, respectively) (see **Figure 9**). Moreover, because grey pumice has more evolved glass and plagioclase compositions (see **Figures 6** and **9**) and includes less phenocryst than brown pumice, the grey magma (as the source of grey pumice) was likely positioned in the relatively upper magma portion, while the brown magma (as the source of brown pumice) was located in the lower portion. This implies that a magma stratification occurred in the more silicic magma prior to the eruption (e.g. **Bacon and Druitt 1988, Ginibre et al., 2004, Suhendro et al., 2021**). The fact that grey magma had a

higher pheno-bubble fraction than brown magma (represented fPV by in pyroclast; see **Figure 8c**) also does not deny the idea of magma stratification in the silicic reservoir (i.e. buoyancy allows volatiles to migrate upwards and accumulate in the upper reservoir portion; **e.g. Suhendro et al. 2022**). While the less silicic magma is likely stored in a deeper depth due to the absence of the biotite mineral phase, and it has less evolved glass compositions (**Miyaji et al., 2011**). In particular, biotite mineral requires a high oxygen fugacity condition, which is associated with a relatively low temperature and low pressure magmatic conditions, at approximately (less than 200 MPa or 6 km crustal depth (note that silica is inversely proportional to magma temperature and storage pressure; **Toramaru 2006, Yücel, et al., 2014; Bunga Naen et al. 2023**). Moreover, the occurrence of the biotite can be used to assume that the more silicic magma was more water-saturated than the less silicic magma (e.g. **Costa et al., 2013**). This might be the reason why juveniles (grey and brown pumice) from more silicic magma are typically more vesicular compared to scoria from the less silicic magma (see **Figure 8**), as the presence of water becomes the volatile source for second nucleation during magma vesiculation (**Toramaru, 2006**). Noteworthy, it is significant that the biotite compositions and anorthite content of Seminung are different from Ranau (see **Figure 6c**), suggesting that the present Seminung magma reservoirs are independent to that of Ranau caldera, which erupted at ~33.6. ka (**Natawid-**
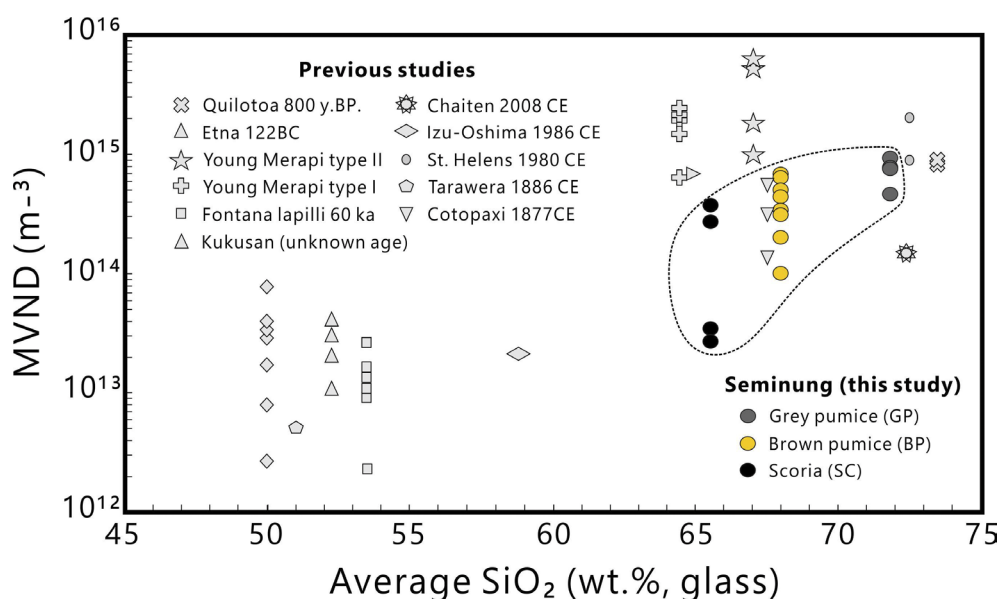
Figure 10: Matrix-vesicle Number Density of Sub-Plinian and Plinian eruptions from basaltic to rhyolitic volcanoes compared with Mt. Seminung. MVND of Seminung's pumice and scoria are comparable with other basaltic to rhyolitic Sub-Plinian/Plinian eruptions from around the world. MVND and glass compositions data are referred to Tarawera 1886 CE eruption (**Constantini et al., 2010**); Izu-Oshima 1986 CE eruption (**Toramaru, 2006**); Fontana Lapilli 60 ka eruption (**Constantini et al., 2010**); Kukusan unidentified eruption age (**Mitsuoka et al., 2021**); Etna 122 BC eruption (**Sable et al., 2006**); Chaitén 2008 eruption (**Alfano et al., 2012**); Cotopaxi layer 1, 2 and 5 (**Alfano et al., 2012**); Quilotoa 800-y B.P. (**Rosi et al., 2004**); St. Helens 1980 CE eruption (**Toramaru 2006**); Type I and type II young Merapi (**Suhendro et al., 2023**) and Seminung (this study), respectively.

jadja et al. 2017) (see **Figure 6c**). The fact that juveniles from Seminung are typically quartz-free also does not deny this idea (see **Figure 6b**). it is also inferred that both magma reservoirs (i.e. the more silicic and less silicic magmas) are probably located at >4 km crustal depth due to the absence of a shallower heat source beneath the volcano (**Maryadi et al., 2022**).

Finally, because a higher temperature forms higher anorthite contents (**Couch et al. 2003**), the reverse zoning textures (as well as sieves and honeycomb texture) in plagioclase of grey and brown pumices (see **Figure 5d-i**) strongly suggest that the temperature of more silicic magma increased (i.e. disequilibrium condition) (**Renjith, 2014**). This interruption might come from the intruding less silicic magma in the lower part of the more silicic magma, causing destabilization and overpressure that is needed to trigger an eruption (**Renjith, 2014**). Moreover, the bimodal anorthite content from brown and grey pumices supports the idea of this process (see **Figure 7**). These results signify that the explosive eruption from Seminung Volcano involves a magma mingling process, such as those observed in the Malinche II pumice eruption of Popocatépetl, the <5 ka eruption of Agnano-Monte Spina, the 550 yr. B.P. eruption of El Misti, the 1875 A.D. eruption of Askja, and the 1914-1915 A.D. eruption of Sakurarjima (**Sigurdsson and Sparks 1981; Macías et al., 2003; Andrews et al., 2008; Tepley et al., 2013; Araya et al., 2019; Mangler et al., 2020; Espinosa et al., 2021; Pelulollo et al., 2022;**).

5.3. Eruption dynamics

As mentioned in the previous section, two important phenomena were observed in the pre-eruptive magmatic system beneath Mount Seminung: (1) pheno-bubble stratification and (2) magma mingling-mixing. Both processes are capable of providing magma overpressure (**e.g. Caricchi et al. 2014, Edmonds and Woods 2018, Suhendro et al. 2022**), hence might be the most plausible options for triggering the explosive eruption of Seminung. As magma erupts, sudden decompression occurs, thus resulting in the formation of matrix-bubbles via second nucleation (**e.g. Toramaru 2006**). Since supersaturation of matrix-bubble is effectively diminished by pheno-bubble (**Toramaru 2014, Suhendro et al. 2022**), the earliest eruption with the highest pheno-bubble fraction produces juveniles with the lowest MVND value ($0.2–4.0 \times 10^{14}$ m^{-3}) (see **Figures 8d** and **e**). These MVND values are actually enough to produce a buoyant eruption plume (**e.g. Sable et al. 2006, Constantini et al. 2009**); thus, a possibly large conduit size might be responsible for the formation of PDC instead of pyroclastic fall (**Wilson 1980**). As the MVND increased ($0.3–8.5 \times 10^{14}$ m^{-3} for unit 2 and $2.0–7.0 \times 10^{14}$ m^{-3} for unit 3) due to the decreasing pheno-bubble fraction (see **Figures 8d** and **e**), the eruption began to form pyroclastic fall deposits such as those observed in the remaining units. This means that the eruption reached its peak towards the final eruption stage.

In addition, the values of MVND represent the second nucleation of bubbles during eruption (**Toramaru 2006**). The second nucleation of bubbles is a function of silica content (**Toramaru, 2006**); hence, the values of MVND have a strong dependence on magma compositions. For instance, MVNDs of the Tarawera 1886, Etna 122 BC, and Fontana Lapilli are relatively small ($10^{13\text{-}14}$ m^{-3}) because they have basaltic – basaltic andesite composition, while MVNDs of Chaitén, Quilotoa 800 B.P., and Sakurajima are higher ($10^{14\text{-}15}$ m^{-3}) because of their andesitic-rhyolitic composition (see **Figure 10**). The studied deposits had andesitic to dacitic glass compositions; thus, it is natural that the juveniles from the Seminung eruption (MVNDs of $10^{13\text{-}15}$ m^{-3}) are comparable to the aforementioned silicic sub-Plinian and Plinian eruptions (see **Figure 10**).

6. Conclusions

This study determined the magmatic system and eruption dynamics of the youngest pyroclastic deposits at Mount Seminung using fieldwork-stratigraphy observation, grain size distribution, componentry, petrography, and chemical and textural analyses. The eruption was divided into three units: (1) massive block and ash, (2) interbedded ash and lapilli, and (3) massive lapilli. Each unit includes brown and grey pumice, scoria, and cognate lithics with the occasional banded pumice while accretionary lapilli is an exclusive product of unit 2. Based on the deposit characteristics and stratigraphy, unit 1 and unit 3 likely originated from magmatic-sub-Plinian eruptions, while unit 2 requires further examination because the presence of accretionary lapilli may either suggest direct contact between external water with magma or rainfall-induced agglutination. This eruption started with a low magnitude eruption of initial phase producing PDC (unit 1), followed by a water-involved eruption of lithic-rich alternating ash-lapilli fall (unit 2), and continued by a stable high magnitude eruption stage exhibiting a pumice-rich lapilli fall layer (unit 3). Data from petrography observation, as well as the glass and mineral composition of each juvenile material suggest the occurrence of two magma reservoirs: the biotite-bearing more silicic magma and biotite-free less silicic magma. Abundant fine-sieve, reverse zoning, and honeycomb textures as well as bimodal anorthite content in plagioclase found in grey and banded pumice suggest that mafic magma intruded the lower portion of more silicic magma, causing magma mingling. This process, coupled with the supersaturation of preexisting bubbles (pheno-bubble) in the top of the more silicic magma reservoir likely provides magma overpressure that is needed for triggering the eruption. Finally, the intensity of matrix-bubble nucleation (via second nucleation) during sudden decompression controls the eruption intensity (i.e. higher matrix-vesicle number density increases the explosivity). This means that our awareness of this volcano must be increased because Mount Seminung has been capable of producing explosive eruptions. Furthermore, it is important to do more assessment of its activity by enhancing the monitoring system and expanding the observation points around this volcano.

7. References

Acocella, V., Bellier, O., Sandri, L., Sébrier, M., Pramumijoyo, S. (2018): Weak tectono-magmatic relationships along an obliquely convergent plate boundary: Sumatra, Indonesia, Frontiers in Earth Science, 6:3.

Afiat, Idianto, O., Rera, G.F., Wardoyo, G.K., Sutopo, Pratama, H.B., and Hamdan, M.H. (2021): Updated conceptual model and resource assessment using numerical reservoir simulation of Danau Ranau geothermal field Indonesia, IOP Conf. Series: Earth and Environmental Science, 732, 1-14.

Alfano, F., Bonadonna, C., Volentik, A.C.M., Connor, C.B., Watt, S.F.L., Pyle, D.M., and Connor, L.J. (2011): Tephra stratigraphy and eruptive volume of the May, 2008, Chaitén eruption, Chile, Bull. Volcanol., 73, 613 – 630.

Alfano, F., Bonadonna, C., and Gurioli, L. (2012): Insights into eruption dynamics from textural analysis: the case of the May, 2008, Chaitén eruption, Bull. Volcanol., 74, 2095 – 2108.

Amin, T.C., Santosa, S., and Gunawan, W. (1993) Geological map of the Kotaagung quadrangle, Geological Research and Development Centre.

Andrews, B.J. (2014) Magmatic storage conditions, decompression rate, and incipient caldera collapse of the 1902 eruption of Santa Maria Volcano, Guatemala, Journal of Volcanology and Geothermal Research, 282,103-114.

Andrews, B.J., Gardner, J.E., and Housh, T.B. (2008) Repeated recharge, assimilation, and hybridization in magmas erupted from El Chichon as recorded by plagioclase and amphibole phenocrysts, Journal of Volcanology and Geothermal Research, 175, 415-426.

Araya, N., Nakamura, M., Yasuda, A., et al. (2019): Shallow magma pre-recharge during repeated Plinian eruptions at Sakurajima volcano, Scientific Reports, 9, 1979, 1-10.

Bacon, C.R., and Druitt, T.H. (1988): Compositional evolution of the zoned calcalkaline magma chamber of Mount Mazama, Crater Lake, Oregon, Contrib. Mineral. Petrol., 98, 224-256.

Bellier, O., and Sébrier, M. (1994): Relationship between tectonism and volcanism along the Great Sumatran Fault

Zone deduced by SPOT image analyses, Tectonophysics, 233, 215 – 231.

Bunga Naen, G.N.R., Toramaru, A., Juhri, S., Yonezu, K., Wibowo, H.E., Gunawan, R.M.P.P., and Disando, T. (2023): Distinct pumice populations in the 74 ka Youngest Toba Tuff: Evidence for eruptions from multiple magma chambers, Journal of Volcanology and Geothermal Research 437, 107804.

Cashman, K.V., and Giordano, G. (2014): Review: Calderas and magma reservoirs, J. Volcanology and Geothermal Research, 2, 88, 28 – 45.

Castro, J.M., and Dingwell, D.B. (2009): Rapid ascent of rhyolitic magma at Chaitén volcano, Chile, Nature Letters, 461:8, 780-784.

Castro, J.M., and Feisel, Y. (2022): Eruption of ultralow-viscosity basanite magma at Cumbre Vieja, La Palma, Canary Islands, Nature Communications, 13:3174

Castruccio, A., Clavero, J., Segura, A., Samaniego, P., Roche, O., Le Pennec, J.L., Droguett, B. (2016): Eruptive parameters and dynamics of the April 2015 sub-Plinian eruptions of Calbuco volcano (southern Chile), Bull. Volcanol., 78:62.

Coltelli, M., Carlo, P.D., Vezzoli, L. (1988): Discovery basaltic eruption of Roman age at Etna volcano, Italy, Geology, 26, 12, 1095-1098.

Costa, F., Andreastuti, S., de Maisonneuve, B.D., and Pallister, J.S. (2013): Petrological insights into the storage conditions, and magmatic processes that yielded the centennial 2010 Merapi explosive eruption, Journal of Volcanology and Geothermal Research 261, 209-235.

Couch, S., Harford, C.L., Sparks, R.S.J., and Carroll, M.R. (2003): Experimental constraints on the conditions of formation of highly calcic plagioclase microlites at the Soufriére Hills volcano, Monterrat, Journal of Petrology, 44, 8, 1455-1475.

Edmonds, M., Cashman, K.V., Holness, M., et al. (2018): Architecture and dynamics of magma reservoirs, Phil. Trans. R. Soc. A, 377, 20180298, 1-29.

Espinosa, V.D., Arce, J.L., and Castro-Govea, R. (2021): Pre-eruptive conditions and reheating of dacitic magma (Malinche Pumice II Plinian eruption) at La Malinche volcano, Central Mexico, Journal of Volcanology and Geothermal Research, 419:107368.

Gafoer, S., Amin, T.C., and Pardede, R., Geological map of the Baturaja Quadrangle, Sumatera, Bandung: Geological Research and Development Centre, 1993.

Ginibre, C., Wörner, G., and Kronz, A. (2004): Structure and dynamics of the Laacher See magma chamber (Eifel, Germany) from major and trace element zoning in sanidine: a cathodoluminescence and electron microprobe study, Journal of Petrology, 45, 11, 2197-2223.

Gunawan, H., Surono, Budianto, A., Kristianto, Prambada, O., McCausland, W., Pallister, J., Iguchi, M. (2019): Overview of the eruptions of Sinabung Volcano, 2010 and 2013-present and details of the 2013 phreatomagmatic phase, Journal of Volcanology and Geothermal Research 382, 103-119.

Gunawan, R.M.P.P. (2020): Physical and textural characteristics of Ranau Ignimbrite, Southern Sumatra, Indonesia. Master Thesis, Kyushu: Kyushu University.

Jones, T.J., Beckett, F., Bernard, B., Breard, E. C. P., Dioguardi, F., Dufek, J., Engwell, S., Eychenne, J. (2023): Physical properties of pyroclastic density currents: relevance, challenges and future directions, Frontiers in Earth Science, 11:1218645, 1-21.

Klug, C., and Cashman, K.V. (1994): Vesiculation of May 18, 1980, Mount St. Helens magma, Geology, 22, 468 – 472.

Klug, C., and Cashman, K.V. (1996): Permeability development in vesiculating magmas: implications for fragmentation, Bull. Volcanol. 58, 87 – 100.

Kriswati, E., Meilano, I., Iguchi, M., Abidin, H.Z., Surono. (2019): An evaluation of the possibility of tectonic triggering of the Sinabung eruption, Journal of Volcanology and Geothermal Research 382, 224– 232.

Kusuma, D.S., Widodo, S., Bakrun, et al. (2005): Prospek panas bumi di daerah danau ranau, Lampung dan Sumatera Selatan (*Geothermal prospect in Danau Ranau area, Lampung and South Sumatera*) in: Prosiding Kolokium Hasil Lapangan – DIM, 391-398.

Lamb, O.D., Gestrich, J.E., Barnie, T.D., Jonsdottir, K., Ducrocq, C., Shore, M.J., Lees, J.M., Lee, S.J. (2022): Acoustic observations of lava fountain activity during the 2021 Fagradalsfjall eruption, Iceland, Bull. Volcanol. 84:96.

Maeno, F., Nakada, S., Yoshimoto, M., Shimano, T., Hokanishi, N., Zaennudin, A., and Iguchi, M. (2019): A sequence of a plinian eruption preceded by dome destruction at Kelud volcano, Indonesia, on February 13, 2014, revealed from tephra fallout and pyroclastic density current deposits, Journal of Volcanology and Geothermal Research 382:24-41.

Maeno, F., Shohata, S., Suzuki, Y., Hokanishi, N., Yasuda, A., Ikenaga, Y., Kaneko, T., and Nakada, S. (2023): Eruption style transition during the 2017-2018 eruptive activity at the Shinmoedake volcano, Kirishima, Japan: surface phenomena and eruptive products, Earth and Planets and Space. 75:76.

Macías, J.L., Arce, J.L., Mora, J.C., Espindola, J.M., and Saucedo, R. (2003): A 550-year-old eruption at El Chichon Volcano, Chiapas, Mexico: Explosive volcanism linked to reheating of the magma reservoir, J. Geophysical Res., 108(B12):2569.

Mangler, M.F., Petrone, C.M., Hill, S., Delgado-Granados, H., and Prytulak, J. (2020): A pyroxenic view on magma hybridization and crystallization at Popocatepetl volcano, Mexico, Front. Earth. Sci. 8:32.

Maryadi, M., Firdaus, A., Zarkasyi, A., et al. (2022): Electrical resistivity structure of Danau Ranau geothermal prospect area based on integrated 3-D Inversion of impedance tensor and tipper vector, Geothermics, 106, 102575, 1-10.

Miyaji, N., Kan'no, A., Kanamaru, T., et al. (2011): High-resolution reconstruction of the Hoei eruption (AD 1707) of Fuji volcano, Japan, J. Volcanology and Geothermal Research, 207, 113-129.

Muller, A.V., Cashman, K.V., Mitchell, S.J., and Vasconez, F.J. (2022): The 2.6-2.3 ka explosive eruptive period of the Pu-

lulahua dome complex, Ecuador: insights from pyroclast analysis, Bull. Volcanol., 84:81.

Natawidjaja, D.H., Bradley, K., Daryono, M.R., et al. (2017): Late quaternary eruption of the Ranau caldera and new geological slip rates of the Sumatran Fault Zone in Southern Sumatra, Indonesia, Geosci. Lett. 4, 21, 1-15.

Pelulollo, C., Chakraborty, S., Cambeses, A., Dohmen, R., Arienzo, I., D'Antonio, M., Pappalardo, K., and Petrosino, P. (2022): Insights into the temporal evolution of magma plumbing systems from compositional zoning in clinopyroxene crystals from the Agnano-Monte Spina Plinian eruption (Campi Flegrei, Italy), Geochimica et Cosmochimica Acta, 328, 185-206.

Rolandi, G., Munno, R., Postiglione, I. (2004): The A.D. 472 eruption of the Somma volcano, Journal of Volcanology and Geothermal Research, 129, 219-319.

Rosi, M., Landi, P., Polacci, M., et al. (2004): Role of conduit shear on ascent of the crystal-rich magma feeding the 800-year B.P. Plinian eruption of Quilotoa volcano (Ecuador), Bull. Volcanol., 66, 307 – 321.

Shea, T. (2017): Bubble nucleation in magmas: A dominantly heterogeneous process?, Journal of Volcanology and Geothermal Research, 343, 155-170.

Siebe, C., Salinas, S., Arana-Salinas, L., Macías, J.L., Gardner J., Bonasia, R. (2017): The ~23,500 y 14C BP White Pumice Plinian eruption and associated debris avalanche and Tochimilco lava flow of Popocatépetl, Journal of Volcanology and Geothermal Research, 333-334, 65-95.

Sigurdsson, H (2000): Encyclopedia of Volcanoes, Academic Press.

Sigurdsson, H., and Sparks, R.S.J. (1980): Petrology of rhyolitic and mixed magma ejecta from the 1875 eruption of Askja, Iceland, Journal of Petrology, 22, 41-84.

Suhendro, I., Toramaru, A., Miyamoto, T., Miyabuchi, Y., and Yamamoto, T. (2021): Magma chamber stratification of the 1815 Tambora caldera-forming eruption, Bull. Volcanol., 83, 63, 1-20.

Suhendro, I., Toramaru, A., Harijoko, A., et al. (2022): The origins of transparent and non-transparent white pumice: A case study of the 52 ka Maninjau caldera-forming eruption, Indonesia, J. Volcanology and Geothermal Research, 431, 107643, 1-17.

Suhendro, I., Bunga Naen, G. N. R., Gurusinga, A., Sari, S. A., Moktikanana, M. L. A., Gunawan, R. M. P. P., Jane, J., Qodri, M. F., Sya'bana, F., Cahyani, S. M., Ardian, D. N. (2023): Dynamics of the Young Merapi (<2.2 ka – 1,788 CE) pumice fall deposits: Insights from textural and geo-

chemical studies, J. Volcanology and Geothermal Research, 443, 107919, 1-22.

Tajima, Y., Tamura, K., Yamakoshi, T., Tsune, A., and Tsurumoto, S. (2013): Ellipse-approximated isopach maps for estimating ashfall volume at Sakurajima Volcano, Bull. Volcanol. Soc. Japan, 58, 1, 291-306.

Takahashi, R., Nakagawa, M. (2013): Formation of a compositionally reverse zoned magma chamber: Petrology of the AD 1640 and 1694 eruptions of Hokkaido-Komagatake volcano, Japan, Journal of Petrology, 54, 4, 815 -838.

Takahashi, R., Nakagawa, M. (2013): Formation of a compositionally reverse zoned magma chamber: Petrology of the AD 1640 and 1694 eruptions of Hokkaido-Komagatake volcano, Japan, Journal of Petrology, 54, 4, 815 -838.

Tepley, F.J., da Silva, S., and Salas, G. (2013): Magma dynamics and petrological evolution leading to the VEI 5 2000 BP eruption of El Misti Volcano, Southern Peru, Journal of Petrology 54, 2033-2065.

Toramaru, A. (2006): BND (bubble number density) decompression rate meter for explosive volcanic eruptions, Journal of Volcanology and Geothermal Research, 154, 303-316.

Toramaru, A. (2014): On the second nucleation of bubbles in magmas under sudden decompression, Earth and Planetary Science Letters, 404, 190-199.

Trafton, K.R., Glachetti, T. (2022): The pivotal role of Vulcanian activity in ending the explosive phase of rhyolitic eruptions: the case of the Big Obsidian Flow eruption (Newberry Volcano, USA), Bull. Volcanol., 84:104, 1-18.

Walker, G.P.L., and Croasdale, R. (1971): Characteristics of some basaltic pyroclastics, J. Geol. Soc. London, 127, 17 – 55.

Walker, G.P.L., Self, S., Wilson, L. (1984): Tarawera 1886, New Zealand- a basaltic Plinian fissure eruption, Journal of Volcanology and Geothermal Research 21, 61-78.

Westerveld, J. (1952): Quaternary volcanism on Sumatra, Bull. Geol. Soc. Am., 63, 562-589.

Yücel, C., Arslan, M., Temizel, İ., Abdioğlu, E. (2014): Volcanic facies and mineral chemistry of Tertiary volcanics in the northern part of the Eastern Pontides, northeast Turkey: implications for pre-eruptive crystallization conditions and magma chamber processes, Mineralogy and Petrology, 10, 439-467.

URL https://volcano.si.edu/volcano.cfm?vn=261251 (accessed 2nd September 2022).

URL https://volcano.si.edu/volcano.cfm?vn=261080 (accessed 19th December 2022).

SAŽETAK

Kemijska i teksturna istraživanja najmlađih piroklastičnih naslaga na planini Seminung (Južna Sumatra, Indonezija): okvir za razumijevanje ponašanja vulkana nakon stvaranja kaldere

Najmlađe naslage tefre vulkana Seminung u južnoj Sumatri, Indonezija, proučavane su istraživanjem stratigrafije (terenski podatci), sastavom, petrografijom stakla i minerala te analizom teksture vezikula kako bi se interpretirao magmatski sustav i dinamika erupcija. Na temelju sastava i granulometrijskih karakteristika vulkanoklastičnih čestica snimljeni slijed podijeljen je u tri različite jedinice: (1) masivni blokovi i pepeo, (2) proslojavanje pepela i lapila te (3) masivni lapili. Sve jedinice sadržavaju sivi plovućac (GP), smeđi plovućac (BP) i skoriju (SC) kao glavne juvenilne čestice, dok se klasti porfirne lave pojavljuju kao nejuvenilna faza (litični fragmenti). Rjeđe je u svim jedinicama zabilježena i pojava trakastoga plovućca (BaP), dok se akrecijski lapili (AL) isključivo nalaze u jedinici proslojavanja pepela i lapila. Mineraloške sličnosti i linearna korelacija između svih glavnih elemenata u sastavu vulkanskoga stakla upućuju na to da su sivi i smeđi plovućac došli iz iste plitke, biotitom bogate magme s višim udjelom silicijske komponente (64,5 – 74,9 wt % SiO_2^{glass}), dok skorija potječe iz dublje, biotita lišene magme nižega sadržaja silicijske komponente (62,1 – 69,2 wt % SiO_2^{glass}). Činjenica da sivi plovućac pokazuje više vrijednosti sadržaja silicijske komponente i frakciju feno-mjehurića s nižim sadržajem fenokristala nego smeđi plovućac upućuje na postojanje grube stratifikacije magmatskoga rezervoara koja sadržava više silicija. Nadalje, u magmu s višim sadržajem silicijske komponte vjerojatno je prodirala silicijskom komponentom siromašnija magma s većih dubina, na što upućuje bimodalna raspodjela anortita (An#) u sivim i smeđim plovućcima (tj. vrhunac visokoga sadržaja anortita sličan je onomu u skoriji). S obzirom na navedeno, nakupljanje feno-mjehurića i magmatsko punjenje rezervoara vjerojatno su bili odgovorni za pokretanje erupcija. Konačno, činjenica da su juvenilni klastiti iz jedinica 2 i 3 imali najveću gustoću matriksa prema vezikulama (MVND) implicira da je intenzitet erupcije dosegnuo svoj vrhunac prema završnoj fazi erupcije.

Ključne riječi:
Seminung, miješanje magme, slojevitost magme, nadtlak, feno-mjehurić, matriks-vezikule

Author's contribution

Rachmi Mustika Pertiwi Putri Gunawan (1) (M.Sc.) conceptualized the research, conducted fieldwork during April 20th - 23rd, 2019 to collect pyroclastic deposits samples at the NE flank of Seminung Volcano, interpreted the data, prepared a stratigraphic column as well as the basic map, and wrote the initial manuscript. **Indranova Suhendro (2)** (Dr.Sc.) joined the fieldwork, did all laboratory analyses, data curation, and gave critical comments during the writing process. **All authors** contributed to the improvement of the manuscript.